

# Fluid Reconfigurable Intelligent Surface Enabling Index Modulation

Peng Zhang, *Graduate Student Member, IEEE*, Jian Dang, *Senior Member, IEEE*,  
Miaowen Wen, *Senior Member, IEEE*, Ziyang Liu, Kai-Kit Wong, *Fellow, IEEE*,  
Chen Zhao, *Senior Member, IEEE*, Huaifeng Shi, and Zaichen Zhang, *Senior Member, IEEE*

**Abstract**—Fluid reconfigurable intelligent surfaces (FRIS) enable joint position and phase reconfigurability by integrating fluid antennas (FA) with conventional reconfigurable intelligent surfaces (RIS). In this paper, we propose a novel FRIS-based index modulation (IM) framework that exploits the additional spatial degrees of freedom introduced by FRIS element-position reconfiguration. Based on this framework, two transmission schemes are developed, namely FRIS-assisted receiver spatial modulation (FRIS-RSM) and receiver spatial shift keying (FRIS-RSSK), where information bits are conveyed through receiver-antenna index selection. The proposed framework supports both continuous and finite-bit phase control while accounting for FRIS-side spatial correlation. To balance detection complexity and bit error rate (BER) performance, a two-stage reduced-complexity list detector is proposed. For performance analysis under double-Rayleigh cascaded fading with strongest-link selection, tractable post-selection statistics are developed for both continuous-phase and quantized-phase FRIS and incorporated into a moment-generating-function (MGF)-based framework to derive unconditional pairwise error probability (UPEP) and union-bound BER expressions. Simulation results demonstrate significant BER gains over conventional RIS-assisted schemes and verify the accuracy of the analysis.

**Index Terms**—Fluid reconfigurable intelligent surface, index modulation, quantized phase, spatial correlation, performance analysis.

## I. INTRODUCTION

AS wireless communication technologies continue to evolve, future networks are expected to support higher data rates and more reliable transmissions driven by emerging applications such as artificial-intelligence-enabled information

Peng Zhang, Jian Dang, and Zaichen Zhang are with the National Mobile Communications Research Laboratory and the Frontiers Science Center for Mobile Information Communication and Security, Southeast University, Nanjing 211189, China. Jian Dang is also with the Key Laboratory of Intelligent Support Technology for Complex Environments, Ministry of Education, Nanjing University of Information Science and Technology, Nanjing 210044, China. All three authors are also with Purple Mountain Laboratories, Nanjing 211111, China (e-mail: peng\_zhang@seu.edu.cn; dangjian@seu.edu.cn; zczhang@seu.edu.cn).

Miaowen Wen is with the School of Electronic and Information Engineering, South China University of Technology, Guangzhou 510640, China (e-mail: eemwwen@scut.edu.cn).

Ziyang Liu is with the School of Communication Engineering, Hangzhou Dianzi University, Hangzhou 310018, China (e-mail: 251080010@hdu.edu.cn).

Kai-Kit Wong is with the Department of Electronic and Electrical Engineering, University College London, London WC1E 7JE, U.K., and also with the Yonsei Frontier Lab, Yonsei University, Seoul 03722, South Korea (e-mail: kai-kit.wong@ucl.ac.uk).

Chen Zhao and Huaifeng Shi are with the School of Electronics and Information Engineering, Nanjing University of Information Science and Technology, Nanjing 210044, China (e-mail: 002912@nuist.edu.cn; shi-huaifeng@nuist.edu.cn).

Corresponding authors: Jian Dang and Zaichen Zhang (e-mail: dangjian@seu.edu.cn; zczhang@seu.edu.cn).

exchange and sensor-data delivery for intelligent driving [1], [2]. The resulting surge in traffic places increasing pressure on conventional physical-layer designs. In particular, fixed-antenna architectures offer limited spatial adaptability and thus cannot fully exploit the available spatial degrees of freedom (DoF), which restricts their capability to meet the stringent performance requirements of next-generation wireless systems.

Fluid antenna (FA) technology [3]–[5] provides a practical means to introduce spatial reconfigurability into the physical layer and to create additional exploitable DoF within a compact hardware volume. In a fluid-antenna system (FAS), the radiating or receiving point can switch among multiple candidate ports distributed over a compact carrier, thereby forming either a dense discrete set or an effectively continuous aperture. The selected port is adapted to the instantaneous channel state information (CSI) on a per-channel-use basis. Importantly, the FA concept is not tied to a single hardware realization. It can be implemented through mechanically movable antennas [6], liquid radiators controlled by micropumps or electrowetting-on-dielectric (EWOD) techniques [7], pixelated reconfigurable antennas enabled by switch networks such as PIN diodes and micro-electro-mechanical systems (MEMS) [8], [9], or hybrid combinations of these mechanisms [10]. These realizations make spatial reconfigurability feasible even under stringent form-factor constraints and have motivated broad interest in FAS-enabled transmission and networking for future 6G communication systems.

Owing to this additional spatial flexibility, FAS has been investigated in a variety of emerging scenarios. In multiuser systems, fluid antenna multiple access (FAMA) exploits port switching to improve user separability and cell-edge performance [11]–[14]. In integrated sensing and communication (ISAC), joint port selection and waveform or beamforming design enables a controllable sensing-communication trade-off [15], [16]. In near-field communications, adaptive port selection can further enhance energy focusing and user discrimination [17]–[19]. FAS has also been combined with other emerging technologies, such as reconfigurable intelligent surfaces (RISs) [20] and AI-assisted network adaptation [21], to improve robustness in dynamic wireless environments.

Beyond diversity enhancement, FA also opens a new avenue for improving spectral efficiency through index modulation (IM). In position IM (PIM), part of the information bits are mapped to the index of the activated FA position [22]. This idea was later extended from single-position activation to multi-position activation patterns [23], while grouping-based designs were proposed to mitigate the impact of strong spatial correlation among candidate ports [24]. Channel-coded IM for correlated FASs was studied in [25], and differential

IM was developed to avoid relying on instantaneous CSI at the receiver [26]. In addition, covert information embedding through continuous fluid-antenna trajectories was investigated in [27]. These studies show that FA-enabled IM can exploit spatial reconfigurability not only for diversity enhancement but also for carrying additional information bits.

Similarly, RISs provide a passive and low-cost means to reconfigure the wireless propagation environment, and this reconfigurability also enables RIS-assisted IM. RIS-aided receiver spatial modulation (RSM) and receiver spatial shift keying (RSSK) established a new paradigm in which RIS phase adjustments coherently focus multipath components on selected receive antennas, thereby conveying information through receiver-side indices and substantially improving the bit error rate (BER) performance [28]. This paradigm was later extended in several directions, including RIS-assisted transceiver spatial modulation (RIS-TSM) [29], quadrature RSM and quadrature RSSK [30], [31], receiver generalized space-shift keying and receiver generalized spatial modulation [32], as well as enhanced and flexible receiver-side mapping strategies [33]–[35]. By incorporating FAS into RIS-assisted transmission, higher spatial DoF can be harvested to improve robustness and flexibility [36]. Nevertheless, in conventional RIS architectures, the locations of the reflecting elements remain fixed, and hence the spatial reconfigurability of the electromagnetic environment is fundamentally limited.

To overcome this limitation, the recently proposed fluid RIS (FRIS) introduces element-position reconfigurability within each sub-aperture, thereby combining the phase programmability of RIS with the position reconfigurability of FAS and substantially enlarging the controllable spatial DoF [37]. Recent studies have shown that FRIS can adapt its operating mode according to instantaneous CSI and jointly optimize activated element locations, reflection phases, and even active beamforming or spherical-harmonic coefficients [38], [39], leading to improved single-user achievable rate and enhanced multiuser sum rate or capacity [40], [41]. FRIS has also been explored for holographic communications [42] and physical-layer security [43], [44]. However, most existing FRIS studies focus on beamforming, rate, capacity, or secrecy metrics. In contrast, FRIS-assisted modulation design, especially FRIS-enabled IM, remains largely unexplored. More importantly, existing RIS-IM frameworks cannot be directly extended to FRIS, because FRIS introduces joint position-phase reconfiguration, dense-grid spatial correlation, and selection-induced post-processing statistics that fundamentally alter both the transmission design and the performance analysis.

Motivated by this gap, this paper develops a FRIS-assisted IM framework for single-input multiple-output (SIMO) transmission. Specifically, we propose FRIS-assisted RSM and FRIS-assisted RSSK, referred to as FRIS-RSM and FRIS-RSSK, respectively, where the FRIS jointly performs fluid-element selection and phase configuration to focus cascaded signals on designated receive antennas and encode information through receiver-side indices. Compared with conventional RIS-assisted IM, the proposed framework exploits a larger candidate set of reflecting locations under the same active-element budget, thereby unlocking an additional spatial design dimen-

sion. However, realizing and analyzing such a framework is nontrivial for at least three reasons. First, the dense fluid-element grid often leads to sub-wavelength spacing and thus strong spatial correlation, which couples element activation with phase configuration. Second, practical implementations must accommodate both continuous-phase control and finite-resolution phase quantization in a unified manner. Third, FRIS beam focusing relies on strongest-link selection among the candidate cascaded paths under double-Rayleigh fading. The resulting post-selection statistics of the focused equivalent channel, especially in the presence of quantization errors, are difficult to characterize and make the associated BER analysis highly challenging.

To address the above issues, the main contributions of this paper are summarized as follows:

- We propose FRIS-RSM and FRIS-RSSK, a new class of FRIS-enabled IM schemes that exploit joint fluid-element selection and phase configuration to focus cascaded signals on selected receive antennas and convey information through receiver-side indices. The proposed framework supports both continuous-phase control and finite-bit phase quantization, while explicitly incorporating FRIS-side spatial correlation.
- We develop reduced-complexity detectors tailored to the proposed architecture, including a greedy detector and a two-stage reduced-complexity list detector. By first screening candidate receive antennas according to received energies and then restricting the joint search to a short candidate list, the proposed detectors provide a flexible complexity-performance tradeoff and can approach maximum-likelihood (ML) performance with substantially reduced complexity.
- We establish tractable post-selection statistics for FRIS transmission with strongest-link selection over double-Rayleigh cascaded fading. For continuous-phase FRIS, a threshold-based truncated model is used to characterize the selected cascaded-gain statistics. For quantized-phase FRIS, an in-phase projection model is developed to capture the coherent combining loss and quadrature leakage introduced by finite-bit phase quantization.
- Based on the above moment characterization, we derive a moment-generating-function (MGF)-based analytical framework for evaluating the unconditional pairwise error probability (UPEP) and the union-bound BER. In addition, for correlated FRIS channels, we prove that the identity-correlation case  $\mathbf{J} = \mathbf{I}$  serves as a BER lower-bound benchmark under unit-diagonal correlation constraints. Numerical results validate the analysis and demonstrate that the proposed FRIS-enabled IM schemes achieve significant BER gains over conventional RIS-assisted counterparts while offering favorable hardware-complexity-performance tradeoffs.

The rest of this paper is organized as follows. Section II presents the FRIS-assisted SIMO system model and the proposed FRIS-RSM/RSSK transmission and detection schemes with continuous- and quantized-phase configurations. Section III develops an MGF-based UPEP and BER analy-

sis, including tractable post-selection statistics under double-Rayleigh cascaded fading with phase quantization. Section IV presents numerical results that validate the proposed schemes and analysis. Section V concludes this paper, and Appendix A proves the identity-correlation lower-bound benchmark under unit-diagonal correlation constraints.

*Notations:* Bold lowercase and uppercase letters represent vectors and matrices, respectively. The imaginary unit is written as  $j = \sqrt{-1}$ , and  $\mathbf{I}_n$  is the  $n \times n$  identity matrix. For a complex scalar  $x$ ,  $|x|$  and  $\angle(x)$  give its magnitude and phase, and  $\Re\{\cdot\}$  and  $\Im\{\cdot\}$  extract the real and imaginary parts. The operators  $(\cdot)^T$  and  $(\cdot)^H$  stand for transpose and conjugate transpose, respectively. The Euclidean norm and Frobenius norm are written as  $\|\cdot\|_2$  and  $\|\cdot\|_F$ , respectively. The operators  $\text{tr}(\cdot)$ ,  $\det(\cdot)$ ,  $\text{diag}(\cdot)$ , and  $\text{vec}(\cdot)$  refer to the trace, determinant, diagonal formation/extraction, and vectorization, respectively;  $\odot$  is the Hadamard product. The floor operator is denoted by  $\lfloor \cdot \rfloor$ , and  $(x)_{2\pi}$  refers to the modulo- $2\pi$  operation. The expectation and probability operators are  $\mathbb{E}[\cdot]$  and  $\Pr(\cdot)$ , and  $Q(\cdot)$  is the Gaussian  $Q$ -function. A circularly symmetric complex Gaussian random variable follows  $\mathcal{CN}(\mu, \sigma^2)$ , and a real Gaussian random vector follows  $\mathcal{N}(\mu, \mathbf{C})$ . Calligraphic symbols such as  $\mathcal{S}$  and  $\mathcal{X}$  indicate index sets and constellations, respectively;  $\pi(\cdot)$  is a permutation operator. The Bessel function of the first kind of order zero is  $J_0(\cdot)$ , and the modified Bessel functions of the second kind of orders zero and one are  $K_0(\cdot)$  and  $K_1(\cdot)$ , respectively;  $\Gamma(\cdot)$  and  $G_{p,q}^{m,n}(\cdot)$  represent the Gamma and Meijer- $G$  functions.

## II. SYSTEM MODEL

As illustrated in Fig. 1, we consider a FRIS-assisted single-input multiple-output (SIMO) system, where a single-antenna transmitter (Tx) communicates with an  $N_r$ -antenna receiver (Rx) through a FRIS deployed on surrounding buildings. The direct Tx–Rx link is assumed to be blocked by surrounding obstacles. The FRIS acts as a programmable planar aperture that reshapes the impinging electromagnetic wavefront through joint fluid-element activation and phase control. This reconfigurability is exploited to realize the proposed receiver-index-modulated transmission framework.

### A. FRIS Architecture and Spatial Correlation Channel Model

The FRIS is modeled as a uniform planar array (UPA) with  $N_x$  and  $N_z$  candidate fluid elements along the horizontal and vertical dimensions, respectively, yielding a total of  $N_{\text{tot}} = N_x N_z$  candidate elements. The  $n$ -th element is indexed by  $(i_n, j_n)$ , where  $i_n \in \{0, 1, \dots, N_x - 1\}$  and  $j_n \in \{0, 1, \dots, N_z - 1\}$ . Let  $d_x$  and  $d_z$  denote the inter-element spacings along the two axes. Then, the Euclidean distance between the  $p$ -th and  $q$ -th elements is

$$d_{p,q} = \sqrt{d_x^2(i_p - i_q)^2 + d_z^2(j_p - j_q)^2}. \quad (1)$$

Due to the dense fluid-element grid, especially under sub-wavelength spacings, the scattered fields across the FRIS aperture are spatially correlated. In this paper, we focus on FRIS-side spatial correlation, which constitutes the dominant

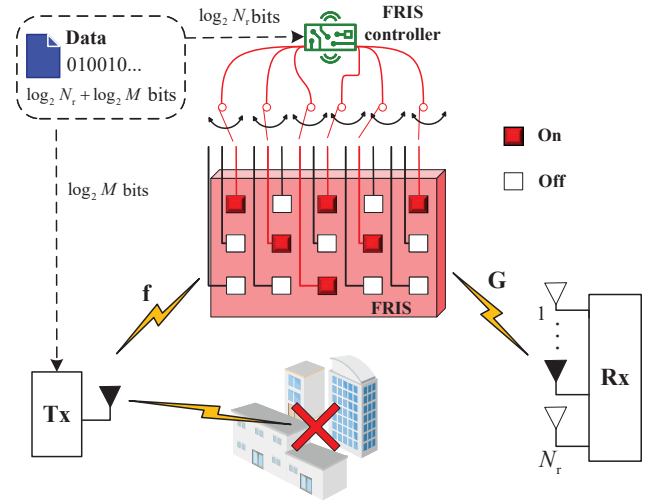


Fig. 1. Block diagram of the proposed FRIS-RSM/RSSK system model.

coupling effect induced by dense fluid-element deployment. Following the classical Jakes model for isotropic scattering environments [45], which has also been widely adopted in FRIS-related studies [40], [41], this spatial correlation is characterized by an  $N_{\text{tot}} \times N_{\text{tot}}$  Hermitian positive semidefinite matrix  $\mathbf{J}$  with unit diagonal entries:

$$\mathbf{J} = \begin{bmatrix} J_{1,1} & J_{1,2} & \cdots & J_{1,N_{\text{tot}}} \\ J_{2,1} & J_{2,2} & \cdots & J_{2,N_{\text{tot}}} \\ \vdots & \vdots & \ddots & \vdots \\ J_{N_{\text{tot}},1} & J_{N_{\text{tot}},2} & \cdots & J_{N_{\text{tot}},N_{\text{tot}}} \end{bmatrix}, \quad (2)$$

whose  $(p, q)$ -th entry is given by

$$J_{p,q} = J_0\left(\frac{2\pi d_{p,q}}{\lambda}\right). \quad (3)$$

Since  $\mathbf{J}$  is Hermitian positive semidefinite, it admits the eigenvalue decomposition  $\mathbf{J} = \mathbf{U}\mathbf{\Lambda}\mathbf{U}^H$ , where  $\mathbf{U}$  is unitary and  $\mathbf{\Lambda} = \text{diag}(\lambda_1, \dots, \lambda_{N_{\text{tot}}})$  contains the non-negative eigenvalues.

Each FRIS element is connected to a centralized controller through a switching network [8]. To reduce the control and hardware overhead, only a subset of fluid elements is activated during each channel use. Let  $\mathbf{s} = [s_1, \dots, s_{N_{\text{tot}}}]^T \in \{0, 1\}^{N_{\text{tot}} \times 1}$  denote the element-selection vector satisfying  $\sum_{n=1}^{N_{\text{tot}}} s_n = K_{\text{sel}}$ ,  $K_{\text{sel}} \leq N_{\text{tot}}$ , where  $s_n = 1$  indicates that the  $n$ -th element is activated and  $s_n = 0$  otherwise. For an active element, the reflection phase is denoted by  $\theta_n \in [0, 2\pi)$ , and the corresponding reflection coefficient is  $\phi_n = e^{j\theta_n}$ . Collecting all coefficients yields  $\boldsymbol{\phi} = [\phi_1, \dots, \phi_{N_{\text{tot}}}]^T \in \mathbb{C}^{N_{\text{tot}} \times 1}$ . Accordingly, the FRIS reflection vector is

$$\mathbf{v} = \text{diag}(\mathbf{s}) \boldsymbol{\phi} \in \mathbb{C}^{N_{\text{tot}} \times 1}. \quad (4)$$

Due to the dense deployment of fluid elements, especially under sub-wavelength spacing, the channels associated with different FRIS elements are spatially correlated [40]. Following the Jakes model, the FRIS-side spatial correlation is

characterized by the matrix  $\mathbf{J}$ . Accordingly, the received signal can be written as

$$\mathbf{y} = \mathbf{G}\mathbf{J}^{\frac{1}{2}}\mathbf{\Phi}\mathbf{f}x + \mathbf{n}, \quad (5)$$

where  $\mathbf{f} \in \mathbb{C}^{N_{\text{tot}} \times 1}$  denotes the underlying Tx-FRIS channel vector,  $\mathbf{G} \in \mathbb{C}^{N_r \times N_{\text{tot}}}$  denotes the underlying FRIS-Rx channel matrix,  $\mathbf{\Phi} = \text{diag}(\mathbf{v})$  is the FRIS reflection matrix, and  $\mathbf{n} \sim \mathcal{CN}(\mathbf{0}, N_0 \mathbf{I}_{N_r})$  is the additive white Gaussian noise vector. For the underlying small-scale fading, we assume  $\mathbf{f} \sim \mathcal{CN}(\mathbf{0}, \mathbf{I}_{N_{\text{tot}}})$  and  $\text{vec}(\mathbf{G}) \sim \mathcal{CN}(\mathbf{0}, \mathbf{I}_{N_r N_{\text{tot}}})$ , with  $\mathbf{f}$  independent of  $\mathbf{G}$ . For notational convenience, we define the equivalent correlated FRIS-Rx channel as  $\tilde{\mathbf{G}} \triangleq \mathbf{G}\mathbf{J}^{\frac{1}{2}}$ , such that (5) can be equivalently rewritten as  $\mathbf{y} = \tilde{\mathbf{G}}\mathbf{\Phi}\mathbf{f}x + \mathbf{n}$ .

### B. FRIS-RSM/RSSK Transmission Framework

In the proposed FRIS-RSM and FRIS-RSSK framework, the FRIS predefines  $N_r$  beamforming modes. The information bits are grouped into blocks of  $B = B_1 + B_2 = \log_2(N_r M)$  bits, denoted by  $\mathbf{b} \in \{0, 1\}^{B \times 1}$ . Specifically,  $B_1 = \log_2 N_r$  bits select a beamforming-mode index  $i \in \{1, \dots, N_r\}$ , which determines the receive antenna on which the FRIS focuses the signal energy, while the remaining  $B_2 = \log_2 M$  bits are mapped to an  $M$ -ary constellation symbol  $x \in \mathcal{X}$ , such as a PSK or QAM symbol. When  $M > 1$ , the scheme corresponds to FRIS-RSM; when  $M = 1$ , the constellation symbol is removed and the scheme reduces to FRIS-RSSK.

Let  $\tilde{g}_{\ell,n} = \alpha_{\ell,n} e^{j\vartheta_{\ell,n}}$  denote the  $(\ell, n)$ -th entry of  $\tilde{\mathbf{G}}$ , and let the Tx-FRIS channel coefficient be written as  $f_n = \beta_n e^{j\omega_n}$ . For beamforming mode  $i$ , the FRIS configuration is specified by the selection vector  $\mathbf{s}_i = [s_{i,1}, \dots, s_{i,N_{\text{tot}}}]^T \in \{0, 1\}^{N_{\text{tot}} \times 1}$  and the phase vector  $\boldsymbol{\theta}_i = [\theta_{i,1}, \dots, \theta_{i,N_{\text{tot}}}]^T$  with  $0 \leq \theta_{i,n} < 2\pi$ . The corresponding reflection vector  $\mathbf{v}_i = [v_{i,1}, \dots, v_{i,N_{\text{tot}}}]^T$  is defined as

$$v_{i,n} \triangleq s_{i,n} e^{j\theta_{i,n}}, \quad 1 \leq n \leq N_{\text{tot}}, \quad (6)$$

or equivalently  $\mathbf{v}_i = \mathbf{s}_i \odot e^{j\boldsymbol{\theta}_i}$ , with the corresponding reflection matrix  $\mathbf{\Phi}_i = \text{diag}(\mathbf{v}_i)$ .

Under mode  $i$ , the cascaded channel coefficient through the  $n$ -th FRIS element toward the  $\ell$ -th receive antenna is defined as

$$c_{\ell,n} \triangleq \tilde{g}_{\ell,n} f_n, \quad 1 \leq \ell \leq N_r, \quad 1 \leq n \leq N_{\text{tot}}, \quad (7)$$

and the corresponding effective cascaded gain at the  $\ell$ -th receive antenna is

$$H_{\ell}^{(i)} \triangleq \sum_{n=1}^{N_{\text{tot}}} c_{\ell,n} v_{i,n}. \quad (8)$$

The received signal at the  $\ell$ -th antenna can thus be expressed as

$$y_{\ell} = H_{\ell}^{(i)} x + n_{\ell}. \quad (9)$$

where  $n_{\ell} \sim \mathcal{CN}(0, N_0)$ . Accordingly, the instantaneous signal-to-noise ratio (SNR) at the  $\ell$ -th receive antenna is

$$\gamma_{\ell} = \frac{E_s}{N_0} |H_{\ell}^{(i)}|^2, \quad (10)$$

where  $E_s \triangleq \mathbb{E}\{|x|^2\}$ .

### C. FRIS Configuration Design

To facilitate the subsequent FRIS configuration design, we define  $h_{\ell,n} \triangleq \alpha_{\ell,n} \beta_n s_{i,n}$  and  $\psi_{\ell,n} \triangleq \vartheta_{\ell,n} + \omega_n + \theta_{i,n}$ . Using the identity  $|\sum_n h_{\ell,n} e^{j\psi_{\ell,n}}|^2 = \sum_n h_{\ell,n}^2 + 2 \sum_{p < q} h_{\ell,p} h_{\ell,q} \cos(\psi_{\ell,p} - \psi_{\ell,q})$ , the SNR expression in (10) can be rewritten as

$$\gamma_{\ell} = \frac{E_s}{N_0} \left( \sum_{n=1}^{N_{\text{tot}}} h_{\ell,n}^2 + 2 \sum_{p=1}^{N_{\text{tot}}} \sum_{q=p+1}^{N_{\text{tot}}} h_{\ell,p} h_{\ell,q} \cos(\psi_{\ell,p} - \psi_{\ell,q}) \right). \quad (11)$$

*1) Continuous-Phase FRIS Design With Strongest-Link Selection:* For beamforming mode  $i$ , the cascaded coefficient associated with the intended antenna through the  $n$ -th fluid element is  $c_{i,n} = \tilde{g}_{i,n} f_n$ . With continuous phase control, the FRIS phases are designed to coherently align the cascaded signals impinging on the intended antenna. Specifically, for an active element  $n \in \mathcal{S}_i$ , the reflection phase is selected according to

$$\theta_{i,n}^* = -\angle(c_{i,n}) \in [0, 2\pi), \quad (12)$$

which ensures that  $c_{i,n} e^{j\theta_{i,n}^*} = |c_{i,n}|$ , i.e., the cascaded contribution becomes real and nonnegative.

Under this phase-alignment rule, maximizing the coherent sum gain at antenna  $i$  reduces to selecting the  $K_{\text{sel}}$  strongest cascaded links according to  $|c_{i,n}|$ . Let  $\pi_i(\cdot)$  denote a permutation of  $\{1, \dots, N_{\text{tot}}\}$  such that

$$|c_{i,\pi_i(1)}| \geq \dots \geq |c_{i,\pi_i(N_{\text{tot}})}|. \quad (13)$$

Then the active-element set is chosen as

$$\mathcal{S}_i \triangleq \{\pi_i(1), \dots, \pi_i(K_{\text{sel}})\}. \quad (14)$$

Accordingly, the configuration coefficients are given by

$$s_{i,n} = \begin{cases} 1, & n \in \mathcal{S}_i, \\ 0, & \text{otherwise,} \end{cases} \quad \theta_{i,n} = \begin{cases} -\angle(c_{i,n}), & n \in \mathcal{S}_i, \\ 0, & \text{otherwise.} \end{cases} \quad (15)$$

Defining  $v_{i,n} \triangleq s_{i,n} e^{j\theta_{i,n}}$ , the resulting focused equivalent sum at antenna  $i$  becomes

$$\sum_{n=1}^{N_{\text{tot}}} \tilde{g}_{i,n} v_{i,n} f_n = \sum_{n \in \mathcal{S}_i} |c_{i,n}|. \quad (16)$$

*2) Quantized-Phase FRIS Design With Strongest-Link Selection:* We next consider a quantized-phase FRIS with  $Q$ -bit phase quantization. The available phase alphabet is

$$\mathcal{A}_Q \triangleq \{0, \Delta, 2\Delta, \dots, (2^Q - 1)\Delta\}, \quad (17)$$

where  $\Delta \triangleq \frac{2\pi}{2^Q}$ .

For beamforming mode  $i$ , the ideal continuous phase alignment follows the compensation rule in (12). Due to the finite-bit phase-quantization constraint, the desired phase is quantized using a modulo- $2\pi$  nearest-angle quantizer with step  $\Delta$ , yielding

$$\theta_{i,n}^{(Q)} = \left( \left\lfloor \frac{(-\angle(c_{i,n}))_{2\pi}}{\Delta} \right\rfloor \Delta + \frac{\Delta}{2} \right)_{2\pi}, \quad (18)$$

where  $(\cdot)_{2\pi}$  denotes the modulo- $2\pi$  operation.

### D. Conditional PDF and Detection

For beamforming mode  $i \in \{1, \dots, N_r\}$ , the FRIS applies the reflection vector  $\mathbf{v}_i = [v_{i,1}, \dots, v_{i,N_{\text{tot}}}]^T$  with the corresponding diagonal reflection matrix  $\Phi_i \triangleq \text{diag}(\mathbf{v}_i)$ . Based on the cascaded channel model with FRIS-side spatial correlation introduced above, the received signal is given by

$$\mathbf{y} = \tilde{\mathbf{G}} \Phi_i \mathbf{f} x + \mathbf{n} = \mathbf{G} \mathbf{J}^{\frac{1}{2}} \Phi_i \mathbf{f} x + \mathbf{n}. \quad (19)$$

1) *Conditional PDF*: Conditioned on the transmitted pair  $(i, x)$  and the channel realization  $(\mathbf{G}, \mathbf{f})$ , it follows from (19) that  $\mathbf{y} \mid (\mathbf{G}, \mathbf{f}, i, x) \sim \mathcal{CN}(\mathbf{G} \mathbf{J}^{\frac{1}{2}} \Phi_i \mathbf{f} x, N_0 \mathbf{I}_{N_r})$ . Therefore, the conditional pdf is given by

$$p(\mathbf{y} \mid \mathbf{G}, \mathbf{f}, i, x) = \frac{1}{(\pi N_0)^{N_r}} \exp\left(-\frac{\|\mathbf{y} - \mathbf{G} \mathbf{J}^{\frac{1}{2}} \Phi_i \mathbf{f} x\|^2}{N_0}\right). \quad (20)$$

2) *ML Detection*: Assuming that  $\mathbf{G}$  and  $\mathbf{f}$  are perfectly known at the receiver, and hence  $\mathbf{G} \mathbf{J}^{\frac{1}{2}} \Phi_i \mathbf{f}$  is known for each mode  $i$ , the optimal maximum-likelihood (ML) detector jointly estimates the beamforming-mode index and the transmitted symbol as

$$\begin{aligned} (\hat{i}, \hat{x}) &= \arg \max_{\substack{i \in \{1, \dots, N_r\} \\ x \in \mathcal{X}}} p(\mathbf{y} \mid \mathbf{G}, \mathbf{f}, i, x) \\ &= \arg \min_{\substack{i \in \{1, \dots, N_r\} \\ x \in \mathcal{X}}} \|\mathbf{y} - \mathbf{G} \mathbf{J}^{\frac{1}{2}} \Phi_i \mathbf{f} x\|^2. \end{aligned} \quad (21)$$

3) *Greedy Detection*: When the FRIS focusing creates a pronounced power disparity across the  $N_r$  receive antennas, a low-complexity greedy detector can be employed. Specifically, the beamforming-mode index is first estimated by selecting the antenna with the largest instantaneous received energy:

$$\hat{i}_G = \arg \max_{\ell \in \{1, \dots, N_r\}} |y_\ell|^2. \quad (22)$$

Given  $\hat{i}_G$ , the transmitted symbol is then detected from the selected branch using a scalar ML rule:

$$\hat{x}_G = \arg \min_{x \in \mathcal{X}} \left| y_{\hat{i}_G} - \left[ \mathbf{G} \mathbf{J}^{\frac{1}{2}} \Phi_{\hat{i}_G} \mathbf{f} \right]_{\hat{i}_G} x \right|^2. \quad (23)$$

The resulting greedy detector has a computational complexity of  $\mathcal{O}(N_r + M)$  and performs well when the intended antenna dominates the remaining branches.

4) *Two-Stage Reduced-Complexity List Detection*: To approach ML performance with reduced search complexity, we construct a reduced-complexity list detector by first forming a candidate list of  $L$  promising beamforming modes based on the received signal energies. Let  $\pi(\cdot)$  denote a permutation of  $\{1, \dots, N_r\}$  such that  $|y_{\pi(1)}|^2 \geq \dots \geq |y_{\pi(N_r)}|^2$ . The Top- $L$  candidate set is then defined as  $\mathcal{M}_L \triangleq \{\pi(1), \dots, \pi(L)\}$ , where  $1 \leq L \leq N_r$ .

In the second stage, the joint search in (21) is restricted to  $i \in \mathcal{M}_L$ , yielding the near-ML decision rule

$$(\hat{i}_L, \hat{x}_L) = \arg \min_{\substack{i \in \mathcal{M}_L \\ x \in \mathcal{X}}} \|\mathbf{y} - \mathbf{G} \mathbf{J}^{\frac{1}{2}} \Phi_i \mathbf{f} x\|^2. \quad (24)$$

The resulting complexity reduces to  $\mathcal{O}(LM)$ , where typically  $L \ll N_r$ . Notably, setting  $L = 1$  yields a single-candidate

near-ML detector, whereas  $L = N_r$  recovers the exact ML detector in (21).

### III. PERFORMANCE ANALYSIS

In this section, we analyze the theoretical BER performance of the proposed FRIS-RSSK/RSM schemes. A fully exact treatment would require characterizing the post-selection distribution of the cascaded-channel magnitudes under Top- $K_{\text{sel}}$  selection in correlated double-Rayleigh fading, which is analytically intractable. To obtain a tractable yet informative benchmark, we therefore focus on the baseline case  $\mathbf{J} = \mathbf{I}$  and use the resulting expressions as a theoretical lower bound for the correlated case, as proved in Appendix A. The analysis proceeds in three steps. First, we express the pairwise error probability in terms of the MGF of the distance metric induced by FRIS-assisted transmission. Second, for continuous- and quantized-phase FRIS, we derive tractable post-selection first- and second-order statistics under strongest-link selection. Third, these effective moments are embedded into an MGF-based UPEP framework, from which the union-bound BER is obtained.

#### A. UPEP Representation via MGF

Given  $\mathbf{G}$ ,  $\mathbf{f}$ , and  $\mathbf{J}$ , the conditional pairwise error probability (CPEP) corresponding to (21) can be written as

$$\begin{aligned} P(i, x \rightarrow \hat{i}, \hat{x} \mid \mathbf{G}, \mathbf{f}, \mathbf{J}) &= P\left(\|\mathbf{y} - \mathbf{G} \mathbf{J}^{\frac{1}{2}} \Phi_i \mathbf{f} x\|_2^2 > \|\mathbf{y} - \mathbf{G} \mathbf{J}^{\frac{1}{2}} \Phi_{\hat{i}} \mathbf{f} \hat{x}\|_2^2\right) \\ &= P\left(\|\mathbf{d}_{i, \hat{i}}^{x, \hat{x}}\|_2^2 + 2 \Re\{\mathbf{n}^H \mathbf{d}_{i, \hat{i}}^{x, \hat{x}}\} < 0\right), \end{aligned} \quad (25)$$

where

$$\mathbf{d}_{i, \hat{i}}^{x, \hat{x}} \triangleq \mathbf{G} \mathbf{J}^{\frac{1}{2}} (\Phi_i \mathbf{f} x - \Phi_{\hat{i}} \mathbf{f} \hat{x}) \in \mathbb{C}^{N_r \times 1} \quad (26)$$

and

$$\mathcal{Z}_{i, \hat{i}}^{x, \hat{x}} \triangleq \|\mathbf{d}_{i, \hat{i}}^{x, \hat{x}}\|_2^2. \quad (27)$$

Using the  $Q$ -function, (25) can be rewritten as

$$P(i, x \rightarrow \hat{i}, \hat{x} \mid \mathbf{G}, \mathbf{f}, \mathbf{J}) = Q\left(\sqrt{\frac{\mathcal{Z}_{i, \hat{i}}^{x, \hat{x}}}{2N_0}}\right). \quad (28)$$

Under the baseline  $\mathbf{J} = \mathbf{I}$ , averaging (28) over the fading channels yields the unconditional pairwise error probability (UPEP),

$$\bar{P}(i, x \rightarrow \hat{i}, \hat{x}) \triangleq \mathbb{E}_{\mathbf{G}, \mathbf{f}} \left[ Q\left(\sqrt{\frac{\mathcal{Z}_{i, \hat{i}}^{x, \hat{x}}}{2N_0}}\right) \right]. \quad (29)$$

Applying Craig's representation  $Q(u) = \frac{1}{\pi} \int_0^{\pi/2} \exp\left(-\frac{u^2}{2 \sin^2 \eta}\right) d\eta$ , (29) can be expressed in terms of MGF

$$\mathcal{M}_{i, \hat{i}}^{x, \hat{x}}(s) \triangleq \mathbb{E}\left[\exp(-s \mathcal{Z}_{i, \hat{i}}^{x, \hat{x}})\right], \quad s \geq 0, \quad (30)$$

as

$$\bar{P}(i, x \rightarrow \hat{i}, \hat{x}) = \frac{1}{\pi} \int_0^{\pi/2} \mathcal{M}_{i, \hat{i}}^{x, \hat{x}}\left(\frac{1}{4N_0 \sin^2 \eta}\right) d\eta. \quad (31)$$

For computational efficiency, we also adopt the accurate two-exponential approximation  $Q(t) \approx \frac{1}{12} \exp\left(-\frac{t^2}{2}\right) + \frac{1}{4} \exp\left(-\frac{2t^2}{3}\right)$  for  $t \geq 0$ , which leads to

$$\bar{P}(i, x \rightarrow \hat{i}, \hat{x}) \approx \frac{1}{12} \mathcal{M}_{i, \hat{i}}^{x, \hat{x}}\left(\frac{1}{4N_0}\right) + \frac{1}{4} \mathcal{M}_{i, \hat{i}}^{x, \hat{x}}\left(\frac{1}{3N_0}\right). \quad (32)$$

Equations (31) and (32) show that the BER analysis reduces to evaluating  $\mathcal{M}_{i, \hat{i}}^{x, \hat{x}}(s)$  for the FRIS-induced cascaded channel under  $\mathbf{J} = \mathbf{I}$ . After separating the real and imaginary parts,  $\mathcal{Z}_{i, \hat{i}}^{x, \hat{x}}$  can be represented as a generalized non-central chi-square random variable associated with an equivalent real Gaussian vector

$$\mathbf{y} \sim \mathcal{N}(\boldsymbol{\mu}, \mathbf{C}), \quad (33)$$

where  $\boldsymbol{\mu}$  and  $\mathbf{C}$  denote the mean vector and covariance matrix determined by the FRIS configuration and the specific error event.

For this generalized non-central chi-square variable, the MGF takes the form [29]

$$\begin{aligned} \mathcal{M}_{i, \hat{i}}^{x, \hat{x}}(s) &= [\det(\mathbf{I} + 2s\mathbf{C})]^{-1/2} \\ &\times \exp\left\{-\frac{1}{2}\boldsymbol{\mu}^T [\mathbf{I} - (\mathbf{I} + 2s\mathbf{C})^{-1}] \mathbf{C}^{-1}\boldsymbol{\mu}\right\}, \end{aligned} \quad (34)$$

where  $(\boldsymbol{\mu}, \mathbf{C})$  depend on the error event  $(i, x) \rightarrow (\hat{i}, \hat{x})$ . Once  $(\boldsymbol{\mu}, \mathbf{C})$  are specified, the corresponding UPEP and the resulting BER follow directly from (34) together with (31)–(32). We next derive the effective first- and second-order statistics required to construct  $(\boldsymbol{\mu}, \mathbf{C})$  for continuous- and quantized-phase FRIS under the analytically tractable baseline  $\mathbf{J} = \mathbf{I}$ .

### B. Continuous-Phase FRIS: Truncated Double-Rayleigh Statistics

We first characterize the per-element statistics under the baseline  $\mathbf{J} = \mathbf{I}$ . From the system model in Section II,  $\tilde{g}_{i,n}$  and  $f_n$  are independent and identically distributed as  $\mathcal{CN}(0, 1)$ . Recalling the cascaded coefficient  $c_{\ell,n}$  defined in (7), the per-element cascaded coefficient toward the focusing antenna  $i$  is  $c_{i,n}$ . Define its magnitude  $r_{i,n} \triangleq |c_{i,n}|$ , which follows the standard double-Rayleigh amplitude distribution with pdf

$$f_r(r) = 4rK_0(2r), \quad r \geq 0, \quad (35)$$

With continuous-phase FRIS, strongest-link selection is performed among the  $N_{\text{tot}}$  candidate cascaded paths according to  $\{r_{i,n}\}$ , where  $K_{\text{sel}}$  elements are activated. Since the exact order statistics are analytically intractable, we adopt a threshold-based approximation and model the selected magnitudes as i.i.d. samples drawn from the tail event  $\{r > \tau_r\}$ , with selection ratio

$$p_{\text{sel}} \triangleq \frac{K_{\text{sel}}}{N_{\text{tot}}}. \quad (36)$$

Accordingly, the threshold  $\tau_r$  is determined by

$$\Pr(r > \tau_r) = p_{\text{sel}}. \quad (37)$$

Using (35), the tail probability admits the closed-form expression

$$\Pr(r > t) = \int_t^\infty 4rK_0(2r) dr = 2tK_1(2t), \quad t \geq 0, \quad (38)$$

so that  $\tau_r$  is obtained by solving  $2\tau_r K_1(2\tau_r) = p_{\text{sel}}$  via a one-dimensional root search, e.g., by using `fzero`.

To build a tractable moment-matching model for the selected magnitudes, we define the incomplete moments over the tail event  $\{r > \tau_r\}$ . In particular,

$$M_0(\tau_r) \triangleq \int_{\tau_r}^\infty 4rK_0(2r) dr = 2\tau_r K_1(2\tau_r), \quad (39)$$

$$\begin{aligned} M_2(\tau_r) &\triangleq \int_{\tau_r}^\infty 4r^3 K_0(2r) dr \\ &= 2\tau_r^3 K_1(2\tau_r) + 2\tau_r^2 K_0(2\tau_r) + 2\tau_r K_1(2\tau_r), \end{aligned} \quad (40)$$

and

$$M_1(\tau_r) \triangleq \int_{\tau_r}^\infty 4r^2 K_0(2r) dr. \quad (41)$$

The integral in (41) can be expressed in closed form using the Meijer- $G$  function. Recall that the Meijer- $G$  function is defined by the Mellin–Barnes integral

$$\begin{aligned} G_{p,q}^{m,n} \left( z \mid \begin{matrix} a_1, \dots, a_p \\ b_1, \dots, b_q \end{matrix} \right) \\ \triangleq \frac{1}{2\pi j} \int_{\mathcal{L}} \frac{\prod_{i=1}^m \Gamma(b_i + s) \prod_{i=1}^n \Gamma(1 - a_i - s)}{\prod_{i=m+1}^q \Gamma(1 - b_i - s) \prod_{i=n+1}^p \Gamma(a_i + s)} z^{-s} ds, \end{aligned} \quad (42)$$

and (41) can be written as

$$M_1(\tau_r) = \tau_r^3 G_{2,4}^{4,0} \left( \tau_r^2 \mid \begin{matrix} -1, -\frac{1}{2} \\ -\frac{3}{2}, -1, 0, 0 \end{matrix} \right), \quad (43)$$

which can be numerically evaluated using standard symbolic or numeric packages, e.g., MATLAB's Symbolic Math Toolbox via `meijerG`.

With  $M_0(\tau_r)$ ,  $M_1(\tau_r)$ , and  $M_2(\tau_r)$ , the truncated first and second moments of the selected magnitudes are

$$\mu_r(\tau_r) \triangleq \mathbb{E}[r \mid r > \tau_r] = \frac{M_1(\tau_r)}{M_0(\tau_r)}, \quad \mathbb{E}[r^2 \mid r > \tau_r] = \frac{M_2(\tau_r)}{M_0(\tau_r)}. \quad (44)$$

The corresponding variance is

$$\sigma_r^2(\tau_r) = \mathbb{E}[r^2 \mid r > \tau_r] - \mu_r^2(\tau_r). \quad (45)$$

Under continuous-phase FRIS, the selected elements are perfectly phase-aligned toward the target antenna, and the coherent combining gain is thus governed by the truncated magnitude statistics in (44)–(45). For later use in the MGF-based UPEP evaluation, we define the corresponding per-element effective statistics as  $\mu_{\text{eff}} = \mu_r(\tau_r)$ ,  $\sigma_{\text{eff}}^2 = \sigma_r^2(\tau_r)$ , and  $E_{\text{eff}}^{(2)} = \mathbb{E}[r^2 \mid r > \tau_r]$ .

### C. Quantized-phase FRIS: Joint Statistics with Phase Quantization

We next consider a practical  $Q$ -bit FRIS, where the phase step is  $\Delta \triangleq \frac{2\pi}{2^Q}$ . Let  $\varepsilon_{i,n} \in [-\Delta/2, \Delta/2]$  denote the quantization error between the ideal continuous alignment phase and the implemented quantized phase for the  $n$ -th

fluid element when focusing on the  $i$ -th receive antenna. As commonly adopted in IM analyses,  $\{\varepsilon_{i,n}\}$  are modeled as i.i.d.  $\mathcal{U}[-\Delta/2, \Delta/2]$  and are assumed to be independent of fading.

Under the baseline  $\mathbf{J} = \mathbf{I}$ , the cascaded coefficient is  $c_{i,n}$  in (7), and its magnitude  $r_{i,n} \triangleq |c_{i,n}|$  follows the double-Rayleigh PDF

$$f_r(r) = 4rK_0(2r), \quad r \geq 0. \quad (46)$$

With phase quantization, only the in-phase projection contributes constructively to coherent combining:

$$a_{i,n} \triangleq r_{i,n} \cos \varepsilon_{i,n}, \quad b_{i,n} \triangleq r_{i,n} \sin \varepsilon_{i,n}. \quad (47)$$

Accordingly, strongest-link selection is performed on  $\{a_{i,n}\}$ , with  $K_{\text{sel}}$  selected elements. As in the continuous-phase case, we approximate the Top- $K_{\text{sel}}$  order statistics by a tail-threshold model, namely, the selected elements are treated as i.i.d. samples conditioned on the event  $\{a > \tau_a\}$ , where  $\tau_a$  is chosen to match the selection ratio  $p_{\text{sel}} \triangleq K_{\text{sel}}/N_{\text{tot}}$ :

$$\Pr(a > \tau_a) = p_{\text{sel}}. \quad (48)$$

A) *Selection probability conditioned on  $r$ .*: Given  $r$ , the event  $\{a > \tau_a\}$  is equivalent to  $\{\cos \varepsilon > \tau_a/r\}$ . Define, for  $r \geq \tau_a$ ,

$$\theta(r) \triangleq \arccos\left(\frac{\tau_a}{r}\right), \quad \phi(r) \triangleq \min\{\theta(r), \frac{\Delta}{2}\}. \quad (49)$$

Since  $\varepsilon \sim \mathcal{U}[-\Delta/2, \Delta/2]$ , we have

$$\Pr(a > \tau_a | r) = \begin{cases} 0, & r \leq \tau_a, \\ \frac{2\phi(r)}{\Delta}, & r > \tau_a. \end{cases} \quad (50)$$

Averaging over  $r$  yields

$$M_0^{(a)}(\tau_a) \triangleq \Pr(a > \tau_a) = \int_{\tau_a}^{\infty} \frac{2\phi(r)}{\Delta} f_r(r) dr, \quad (51)$$

and  $\tau_a$  is obtained by solving  $M_0^{(a)}(\tau_a) = p_{\text{sel}}$  via a one-dimensional root search.

B) *Incomplete moments for  $a$  and  $r$ .*: For  $r > \tau_a$ , the following conditional integrals over  $\varepsilon \in [-\phi(r), \phi(r)]$  are used:

$$\mathbb{E}[\cos \varepsilon \mathbf{1}_{\{a > \tau_a\}} | r] = \frac{2}{\Delta} \sin \phi(r), \quad (52)$$

$$\mathbb{E}[\cos^2 \varepsilon \mathbf{1}_{\{a > \tau_a\}} | r] = \frac{1}{\Delta} (\phi(r) + \frac{1}{2} \sin 2\phi(r)). \quad (53)$$

Hence the key incomplete moments are

$$M_1^{(a)}(\tau_a) \triangleq \mathbb{E}[a \mathbf{1}_{\{a > \tau_a\}}] = \int_{\tau_a}^{\infty} \frac{2r \sin \phi(r)}{\Delta} f_r(r) dr, \quad (54)$$

$$M_2^{(a)}(\tau_a) \triangleq \mathbb{E}[a^2 \mathbf{1}_{\{a > \tau_a\}}] \quad (55)$$

$$= \int_{\tau_a}^{\infty} \frac{r^2}{\Delta} (\phi(r) + \frac{1}{2} \sin 2\phi(r)) f_r(r) dr, \quad (56)$$

$$M_2^{(r)}(\tau_a) \triangleq \mathbb{E}[r^2 \mathbf{1}_{\{a > \tau_a\}}] = \int_{\tau_a}^{\infty} \frac{2r^2 \phi(r)}{\Delta} f_r(r) dr. \quad (57)$$

All integrals above are one-dimensional and can be evaluated numerically; after substituting (46), the integrands involve  $K_0(2r)$  and elementary functions of  $r$ .

C) *Truncated moments and effective parameters.*: The truncated first and second moments of the in-phase projection are given by

$$\begin{aligned} \mu_a(\tau_a) &\triangleq \mathbb{E}[a | a > \tau_a] = \frac{M_1^{(a)}(\tau_a)}{M_0^{(a)}(\tau_a)}, \\ \mathbb{E}[a^2 | a > \tau_a] &= \frac{M_2^{(a)}(\tau_a)}{M_0^{(a)}(\tau_a)}. \end{aligned} \quad (58)$$

and the variance is

$$\sigma_a^2(\tau_a) = \frac{M_2^{(a)}(\tau_a)}{M_0^{(a)}(\tau_a)} - \mu_a^2(\tau_a). \quad (59)$$

The conditional second moment of  $r$  under selection is

$$\mathbb{E}[r^2 | a > \tau_a] = \frac{M_2^{(r)}(\tau_a)}{M_0^{(a)}(\tau_a)}. \quad (60)$$

Since  $r^2 = a^2 + b^2$ , the orthogonal component energy is

$$\begin{aligned} \mathbb{E}[b^2 | a > \tau_a] &= \mathbb{E}[r^2 | a > \tau_a] - \mathbb{E}[a^2 | a > \tau_a] \\ &= \frac{M_2^{(r)}(\tau_a) - M_2^{(a)}(\tau_a)}{M_0^{(a)}(\tau_a)}. \end{aligned} \quad (61)$$

In summary, for quantized-phase FRIS, the per-element effective statistics are characterized by

$$\begin{aligned} \mu_{\text{eff}} &= \mu_a(\tau_a), \quad \sigma_{\text{eff}}^2 = \sigma_a^2(\tau_a), \\ E_{\text{eff}}^{(2)} &= \mathbb{E}[r^2 | a > \tau_a], \quad E_{b,\text{eff}}^{(2)} = \mathbb{E}[b^2 | a > \tau_a]. \end{aligned}$$

Here,  $\mu_{\text{eff}}$  and  $\sigma_{\text{eff}}^2$  characterize the first- and second-order statistics of the in-phase component that contributes constructively to coherent combining,  $E_{\text{eff}}^{(2)}$  captures the total energy of the selected cascaded links, and  $E_{b,\text{eff}}^{(2)}$  quantifies the residual quadrature leakage caused by finite-bit phase quantization. These effective statistics are then incorporated into the mean vector and covariance matrix  $(\boldsymbol{\mu}, \mathbf{C})$  in (34). As  $Q \rightarrow \infty$ , i.e.,  $\Delta \rightarrow 0$ , the phase-quantization error vanishes,  $E_{b,\text{eff}}^{(2)} \rightarrow 0$ , and the above model smoothly reduces to the continuous-phase truncated- $r$  case.

#### D. MGF-Based UPEP Analysis

In this subsection, we tailor (30)–(34) to the proposed FRIS-RSSK/RSM schemes. Owing to the symmetry across receive antennas and the FRIS focusing structure, the error events  $(i, x) \rightarrow (\hat{i}, \hat{x})$  fall into two categories: *i*) index errors with  $i \neq \hat{i}$ , and *ii*) symbol-only errors with  $i = \hat{i}$  and  $x \neq \hat{x}$ . Hence, it suffices to derive the MGF of  $\mathcal{Z}_{i,\hat{i}}^{x,\hat{x}}$  for these two cases. The union bound in (29), or its two-exponential approximation in (32), then follows by summing the corresponding UPEPs weighted by the associated Hamming distances.

Let the effective post-selection statistics of the *per-element* aligned cascaded coefficient be denoted by  $(\mu_{\text{eff}}, \sigma_{\text{eff}}^2, E_{\text{eff}}^{(2)})$  for continuous-phase FRIS and by  $(\mu_{\text{eff}}, \sigma_{\text{eff}}^2, E_{\text{eff}}^{(2)}, E_{b,\text{eff}}^{(2)})$  for quantized-phase FRIS. Specifically, for continuous-phase FRIS,  $\mu_{\text{eff}} = \mu_r(\tau_r)$ ,  $\sigma_{\text{eff}}^2 = \sigma_r^2(\tau_r)$ , and  $E_{\text{eff}}^{(2)} = \mathbb{E}[r^2 | r > \tau_r]$ . For  $Q$ -bit quantized-phase FRIS,  $\mu_{\text{eff}} = \mu_a(\tau_a)$ ,  $\sigma_{\text{eff}}^2 = \sigma_a^2(\tau_a)$ ,  $E_{\text{eff}}^{(2)} = \mathbb{E}[r^2 | a > \tau_a]$ , and  $E_{b,\text{eff}}^{(2)} = \mathbb{E}[b^2 | a > \tau_a]$ , where

$E_{b,\text{eff}}^{(2)}$  characterizes the residual quadrature leakage caused by finite-bit phase quantization. The required truncated moments are given in Sections III-B and III-C. According to the central limit theorem (CLT), the aggregated cascaded gains admit tractable Gaussian approximations when  $K_{\text{sel}}$  is sufficiently large. In particular, after continuous-phase alignment or quantized focusing, the focused equivalent gain  $H_i^{(i)}$  is approximated as a real Gaussian variable whose mean and variance are governed by  $\mu_{\text{eff}}^2$  and  $\sigma_{\text{eff}}^2$ , respectively, whereas each non-focused branch  $H_\ell^{(i)}$ ,  $\ell \neq i$ , is characterized through its second-order energy and is modeled as approximately zero-mean circularly symmetric complex Gaussian. Their corresponding first- and second-order statistics can therefore be approximated as

$$\begin{aligned} \mathbb{E}[H_i^{(i)}] &\approx K_{\text{sel}}\mu_{\text{eff}}, & \text{Var}(H_i^{(i)}) &\approx K_{\text{sel}}\sigma_{\text{eff}}^2, \\ \mathbb{E}[|H_\ell^{(i)}|^2] &\approx K_{\text{sel}}E_{\text{eff}}^{(2)}, & \ell &\neq i. \end{aligned} \quad (62)$$

1) *Case 1: Index Errors  $i \neq \hat{i}$* : For an error event with  $i \neq \hat{i}$ , we rewrite  $\mathcal{Z}_{i,\hat{i}}^{x,\hat{x}}$  in (27) as

$$\mathcal{Z}_{i,\hat{i}}^{x,\hat{x}} = \mathcal{Z}_1^{(1)} + \mathcal{Z}_2^{(1)}, \quad (63)$$

where

$$\mathcal{Z}_1^{(1)} \triangleq |H_i^{(i)}x - H_{\hat{i}}^{(\hat{i})}\hat{x}|^2 + |H_{\hat{i}}^{(i)}x - H_i^{(\hat{i})}\hat{x}|^2, \quad (64)$$

$$\mathcal{Z}_2^{(1)} \triangleq \sum_{\ell=1, \ell \neq i, \hat{i}}^{N_r} |H_\ell^{(i)}x - H_\ell^{(\hat{i})}\hat{x}|^2. \quad (65)$$

Here  $H_\ell^{(i)}$  and  $H_\ell^{(\hat{i})}$  denote the effective cascaded gains at the  $\ell$ -th antenna under the transmitted and competing codewords, respectively. As in [28], [29],  $\mathcal{Z}_1^{(1)}$  collects the two branches directly involved in the index error, whereas  $\mathcal{Z}_2^{(1)}$  aggregates the remaining  $N_r - 2$  branches. For tractability, when a quadratic metric is decomposed into multiple components, we approximate the MGF of the sum by the product of the component MGFs, i.e.,  $\mathcal{M}_{\sum_k \mathcal{Z}_k}(s) \approx \prod_k \mathcal{M}_{\mathcal{Z}_k}(s)$ .

Let  $x = x_R + jx_I$  and  $\hat{x} = \hat{x}_R + j\hat{x}_I$ . Following the moment-matching arguments in Sections III-B–III-C, the real four-dimensional vector

$$\mathbf{y}^{(1)} \triangleq [\Re\{H_i^{(i)}x\}, \Im\{H_i^{(i)}x\}, \Re\{-H_{\hat{i}}^{(\hat{i})}\hat{x}\}, \Im\{-H_{\hat{i}}^{(\hat{i})}\hat{x}\}]^T \quad (66)$$

is approximated as a Gaussian vector,  $\mathbf{y}^{(1)} \sim \mathcal{N}(\boldsymbol{\mu}^{(1)}, \mathbf{C}^{(1)})$ , with mean vector

$$\boldsymbol{\mu}^{(1)} = K_{\text{sel}}\mu_{\text{eff}}[x_R, x_I, -\hat{x}_R, -\hat{x}_I]^T \quad (67)$$

and covariance matrix  $\mathbf{C}^{(1)} \in \mathbb{R}^{4 \times 4}$  given by

$$\mathbf{C}^{(1)} = \begin{bmatrix} \sigma_1^2 & \sigma_{12} & \sigma_{13} & \sigma_{14} \\ \sigma_{12} & \sigma_2^2 & \sigma_{23} & \sigma_{24} \\ \sigma_{13} & \sigma_{23} & \sigma_3^2 & \sigma_{34} \\ \sigma_{14} & \sigma_{24} & \sigma_{34} & \sigma_4^2 \end{bmatrix}, \quad (68)$$

where

$$\begin{aligned} \sigma_1^2 &= K_{\text{sel}}\sigma_{\text{eff}}^2x_R^2 + a_{\hat{x}}, & \sigma_2^2 &= K_{\text{sel}}\sigma_{\text{eff}}^2x_I^2 + a_{\hat{x}}, \\ \sigma_3^2 &= K_{\text{sel}}\sigma_{\text{eff}}^2\hat{x}_R^2 + a_x, & \sigma_4^2 &= K_{\text{sel}}\sigma_{\text{eff}}^2\hat{x}_I^2 + a_x, \\ \sigma_{12} &= K_{\text{sel}}\sigma_{\text{eff}}^2x_Rx_I, & \sigma_{34} &= K_{\text{sel}}\sigma_{\text{eff}}^2\hat{x}_R\hat{x}_I, \\ \sigma_{13} &= c_{\text{eff}}(-x_R\hat{x}_R + x_I\hat{x}_I), & \sigma_{14} &= -c_{\text{eff}}(x_R\hat{x}_I + x_I\hat{x}_R), \\ \sigma_{23} &= \sigma_{14}, & \sigma_{24} &= -\sigma_{13}, \\ a_{\hat{x}} &\triangleq \frac{K_{\text{sel}}E_{\text{eff}}^{(2)}}{2}|\hat{x}|^2, & a_x &\triangleq \frac{K_{\text{sel}}E_{\text{eff}}^{(2)}}{2}|x|^2, & c_{\text{eff}} &\triangleq \frac{K_{\text{sel}}\mu_{\text{eff}}^2}{2}. \end{aligned} \quad (69)$$

Since  $\mathcal{Z}_1^{(1)} = \|\mathbf{y}^{(1)}\|^2$ , its MGF follows directly from (34) as

$$\begin{aligned} \mathcal{M}_{\mathcal{Z}_1^{(1)}}(s) &= [\det(\mathbf{I}_4 + 2s\mathbf{C}^{(1)})]^{-1/2} \\ &\times \exp\left\{-\frac{1}{2}\boldsymbol{\mu}^{(1)T}[\mathbf{I}_4 - (\mathbf{I}_4 + 2s\mathbf{C}^{(1)})^{-1}](\mathbf{C}^{(1)})^{-1}\boldsymbol{\mu}^{(1)}\right\}. \end{aligned} \quad (70)$$

For the remaining  $N_r - 2$  branches, FRIS focusing makes  $H_\ell^{(i)}x - H_\ell^{(\hat{i})}\hat{x}$  approximately zero-mean circularly symmetric complex Gaussian with average energy  $\mathbb{E}[|H_\ell^{(i)}x - H_\ell^{(\hat{i})}\hat{x}|^2] \approx K_{\text{sel}}E_{\text{eff}}^{(2)}(|x|^2 + |\hat{x}|^2)$ . Accordingly,  $\mathcal{Z}_2^{(1)}$  is modeled as the sum of  $N_r - 2$  independent exponential variables, and its MGF is

$$\mathcal{M}_{\mathcal{Z}_2^{(1)}}(s) = \left(1 + sK_{\text{sel}}E_{\text{eff}}^{(2)}(|x|^2 + |\hat{x}|^2)\right)^{-(N_r-2)}. \quad (71)$$

Accordingly, the MGF of  $\mathcal{Z}_{i,\hat{i}}^{x,\hat{x}}$  for Case 1 is

$$\mathcal{M}_{i,\hat{i}}^{x,\hat{x}}(s) \approx \mathcal{M}_{\mathcal{Z}_1^{(1)}}(s) \mathcal{M}_{\mathcal{Z}_2^{(1)}}(s), \quad i \neq \hat{i}. \quad (72)$$

2) *Case 2: Symbol-Only Errors  $i = \hat{i}$* : For symbol-only errors with  $i = \hat{i}$  and  $x \neq \hat{x}$ , the receive-antenna index is detected correctly and the decision metric reduces to the distance between two symbols transmitted over the same equivalent channel. In this case, (27) can be decomposed as

$$\mathcal{Z}_{i,i}^{x,\hat{x}} = \mathcal{Z}_1^{(2)} + \mathcal{Z}_2^{(2)}, \quad (73)$$

where

$$\mathcal{Z}_1^{(2)} \triangleq |H_i^{(i)}(x - \hat{x})|^2, \quad \mathcal{Z}_2^{(2)} \triangleq \sum_{\ell=1, \ell \neq i}^{N_r} |H_\ell^{(i)}(x - \hat{x})|^2. \quad (74)$$

Under the truncated-moment model, the focused equivalent gain at antenna  $i$  is approximated as a real Gaussian random variable  $H_i^{(i)} \sim \mathcal{N}(\mu_H, \sigma_H^2)$ , where  $\mu_H \triangleq K_{\text{sel}}\mu_{\text{eff}}$  and  $\sigma_H^2 \triangleq K_{\text{sel}}\sigma_{\text{eff}}^2$ . Hence,  $\mathcal{Z}_1^{(2)} = |H_i^{(i)}(x - \hat{x})|^2$  is modeled as the scaled square of a non-central real Gaussian variable, whose MGF is

$$\begin{aligned} \mathcal{M}_{\mathcal{Z}_1^{(2)}}(s) &= (1 + 2s\sigma_H^2|x - \hat{x}|^2)^{-1/2} \\ &\times \exp\left(-\frac{\mu_H^2|x - \hat{x}|^2s}{1 + 2s\sigma_H^2|x - \hat{x}|^2}\right). \end{aligned} \quad (75)$$

For each non-focusing branch  $\ell \neq i$ , the cascaded gain satisfies  $H_\ell^{(i)} \sim \mathcal{CN}(0, K_{\text{sel}}E_{\text{eff}}^{(2)})$ , so that  $|H_\ell^{(i)}(x - \hat{x})|^2$  is exponential with mean  $K_{\text{sel}}E_{\text{eff}}^{(2)}|x - \hat{x}|^2$ . Therefore,  $\mathcal{Z}_2^{(2)}$  is Gamma distributed and its MGF is

$$\mathcal{M}_{\mathcal{Z}_2^{(2)}}(s) = \left(1 + sK_{\text{sel}}E_{\text{eff}}^{(2)}|x - \hat{x}|^2\right)^{-(N_r-1)}. \quad (76)$$

Accordingly, the MGF of  $Z_{i,\hat{i}}^{x,\hat{x}}$  for Case 2 is

$$\mathcal{M}_{i,\hat{i}}^{x,\hat{x}}(s) \approx \mathcal{M}_{Z_1^{(2)}}(s) \mathcal{M}_{Z_2^{(2)}}(s), \quad x \neq \hat{x}. \quad (77)$$

Finally, substituting (72) and (77) into (31) or (32), and summing over all codeword pairs with the corresponding Hamming-distance weights yields the desired union bound on the BER for both continuous- and quantized-phase FRIS-RSSK/RSM schemes. The only difference between the two architectures lies in the effective per-element statistics  $(\mu_{\text{eff}}, \sigma_{\text{eff}}^2, E_{\text{eff}}^{(2)})$ , which are provided in Sections III-B and III-C, respectively.

Denote by  $e(i, x \rightarrow \hat{i}, \hat{x})$  the Hamming distance between the bit labels of  $(i, x)$  and  $(\hat{i}, \hat{x})$ . The average bit error probability (ABEP) of the FRIS-RSSK/RSM schemes is then upper-bounded by the classical union bound

$$P_b \leq \frac{1}{MN_r} \sum_{i=1}^{N_r} \sum_{\hat{i}=1}^{N_r} \sum_{x \in \mathcal{X}} \sum_{\hat{x} \in \mathcal{X}} \frac{\bar{P}(i, x \rightarrow \hat{i}, \hat{x}) e(i, x \rightarrow \hat{i}, \hat{x})}{\log_2(MN_r)}, \quad (78)$$

where  $\bar{P}(i, x \rightarrow \hat{i}, \hat{x})$  is obtained from (31) or (32) using the MGFs in (72) and (77).

#### IV. NUMERICAL RESULTS AND DISCUSSION

In this section, numerical results are presented to evaluate the BER performance of the proposed FRIS-assisted RSSK/RSM schemes and to verify the accuracy of the theoretical analysis developed in Section III. Unless otherwise specified, double-Rayleigh fading channels are assumed, and perfect instantaneous CSI is available at the FRIS controller for fluid-element selection and phase configuration. The results are organized to illustrate the impact of the candidate fluid-element grid size, phase-quantization resolution, activation ratio  $K_{\text{sel}}/N_{\text{tot}}$ , the number of activated fluid elements, and the proposed low-complexity Top- $L$  detection scheme. In addition to demonstrating the performance gains of FRIS-enabled IM, these results also reveal the key design tradeoffs among spatial flexibility, hardware overhead, and detection complexity.

Fig. 2 depicts the BER performance of the proposed FRIS-RSSK and FRIS-RSM schemes with a fixed number of controllable RF chains at the FRIS controller, where  $K_{\text{sel}} = 64$  and  $N_r = 4$  for both schemes. For FRIS-RSM, the modulation order is  $M = 16$ . Three FRIS configurations are considered, namely  $(N_{\text{tot}}; N_x, N_z) \in \{(64; 8, 8), (128; 16, 8), (256; 16, 16)\}$ . The reference case  $N_{\text{tot}} = K_{\text{sel}} = 64$  corresponds to the conventional RIS-assisted RSSK/RSM benchmark in [28], where all reflecting elements are actively controlled. To ensure a fair comparison, the physical aperture is kept identical across all configurations by setting  $W_x = W_z = (8 - 1)\lambda/2$ , which corresponds to a half-wavelength-spaced  $8 \times 8$  array for the  $(64; 8, 8)$  configuration. It is observed that enlarging the candidate fluid-element grid yields a clear SNR gain for both FRIS-RSSK and FRIS-RSM. In this experiment,  $N_{\text{tot}}$  increases while  $K_{\text{sel}}$  remains fixed, meaning that the number of active elements and the number of RF control links are unchanged. At a target BER of  $10^{-4}$ , the configuration  $(128; 16, 8)$  achieves an SNR gain

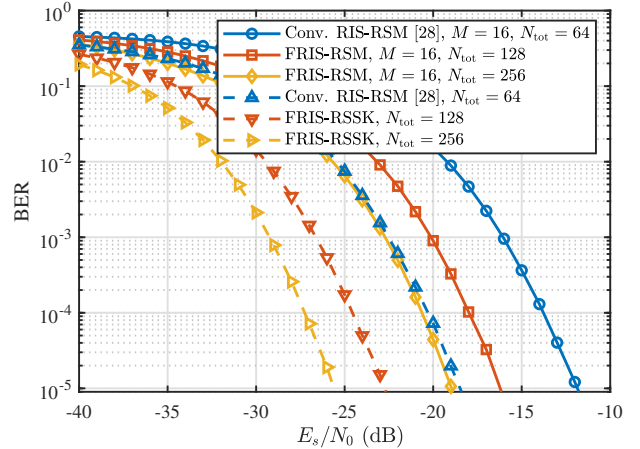


Fig. 2. BER performance comparison of the proposed FRIS-RSSK and FRIS-RSM under different FRIS element-grid sizes  $(N_{\text{tot}}; N_x, N_z) \in \{(64; 8, 8), (128; 16, 8), (256; 16, 16)\}$ , with parameters  $K_{\text{sel}} = 64$  and  $N_r = 4$ .

of about 4.1 dB over the conventional RIS baseline, which further increases to approximately 6.8 dB for  $(256; 16, 16)$ . This result highlights the central advantage of introducing FRIS into the considered IM framework: under the same physical aperture and the same active-element budget, a denser grid of candidate fluid-element locations provides additional spatial DoF for Top- $K_{\text{sel}}$  selection and phase alignment. With instantaneous CSI, the FRIS can exploit this enlarged selection space to identify more favorable cascaded links and coherently focus them toward the intended receive antenna, thereby strengthening the effective cascaded channel and improving the transmission reliability.

Fig. 3 presents the BER performance of the proposed FRIS-RSM scheme under different FRIS configurations and phase-quantization resolutions. The parameters are set to  $(N_{\text{tot}}; N_x, N_z) = (250; 25, 10)$ ,  $K_{\text{sel}} = 50$ ,  $N_r = 4$ , and  $M = 4$ . Two FRIS aperture configurations are considered, namely a dense array with  $(W_x, W_z) = (4.5\lambda, 2\lambda)$  and a sparse array with  $(W_x, W_z) = (9\lambda, 4\lambda)$ , corresponding to a conventional RIS  $10 \times 5$  array with half-wavelength spacing and a  $25 \times 10$  FRIS element grid with unit-wavelength spacing, respectively. The BER performance is evaluated for continuous phase control as well as finite-resolution phase shifts with  $Q = 1, 2, 3$  bits. Several observations can be made from Fig. 3. First, the BER performance of quantized-phase FRIS rapidly approaches that of continuous-phase FRIS as the quantization resolution increases. For the dense configuration  $(4.5\lambda, 2\lambda)$ , the performance loss relative to the continuous-phase case is approximately 2.68 dB, 0.88 dB, and 0.22 dB for  $Q = 1, 2, 3$ , respectively. Similar trends are observed for the sparse configuration  $(9\lambda, 4\lambda)$ , where the corresponding losses are 2.79 dB, 0.94 dB, and 0.28 dB. These results indicate that a small number of quantization bits is already sufficient to recover most of the coherent combining gain. Second, the dense fluid-element array  $(4.5\lambda, 2\lambda)$  consistently exhibits a slight performance degradation compared with the sparse array  $(9\lambda, 4\lambda)$ , due to the stronger spatial correlation among

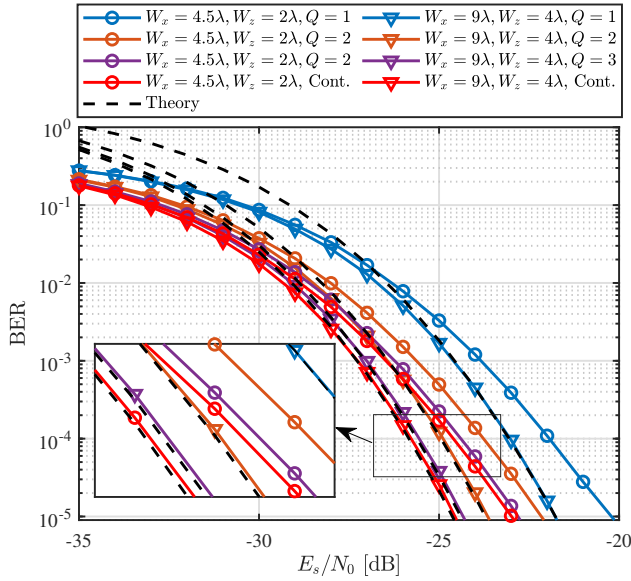


Fig. 3. BER performance comparison of the proposed FRIS-RSM under different phase-shift resolutions and FRIS apertures  $(W_x, W_z) \in \{(4.5\lambda, 2\lambda), (9\lambda, 4\lambda)\}$ , for continuous phase shifts and  $Q \in \{1, 2, 3\}$ -bit quantized phase shifts, with parameters  $(N_{\text{tot}}; N_x, N_z) = (250; 25, 10)$ ,  $K_{\text{sel}} = 50$ ,  $N_r = 4$ , and  $M = 4$ .

neighboring FRIS elements. The corresponding losses are about 1.28 dB, 1.19 dB, 1.17 dB, and 1.12 dB for continuous phase and  $Q = 1, 2, 3$ , respectively. This confirms that spatial correlation weakens the achievable focusing gain, although the overall advantage of FRIS-enabled IM remains evident. Finally, the analytical results closely match the Monte Carlo simulations for the unit-wavelength-spacing case, thereby validating the accuracy of the proposed theoretical framework for both continuous- and quantized-phase configurations.

Fig. 4 shows the simulated and analytical BER performance of the proposed FRIS-RSM scheme for  $(N_{\text{tot}}, K_{\text{sel}}) \in \{(60, 20), (120, 40), (180, 60), (240, 80)\}$ , where  $N_r = 8$  and  $M = 4$ . To ensure a fair comparison across different FRIS sizes, the activation ratio is fixed at  $K_{\text{sel}}/N_{\text{tot}} = 1/3$ , and the inter-element spacings are set to  $d_x = d_z = 2\lambda$  to approximate the weak-correlation regime. The corresponding FRIS geometries are  $(N_x, N_z, W_x, W_z) = (10, 6, 18\lambda, 10\lambda)$ ,  $(12, 10, 22\lambda, 18\lambda)$ ,  $(15, 12, 28\lambda, 22\lambda)$ ,  $(16, 15, 30\lambda, 28\lambda)$ . The results show that increasing  $(N_{\text{tot}}, K_{\text{sel}})$  significantly reduces the required SNR for a given target BER. At  $\text{BER} = 10^{-4}$ , the configurations with  $K_{\text{sel}} = 40, 60$ , and  $80$  achieve SNR gains of 6.41 dB, 10.13 dB, and 12.71 dB, respectively, compared with the baseline  $K_{\text{sel}} = 20$ . This result indicates that when the activation ratio is fixed, increasing both the candidate-set size and the number of active fluid elements provides a compounded benefit: a larger candidate space improves selection diversity, while more activated links further enhance coherent accumulation at the intended receive antenna. Another important observation is that the analytical curves become progressively tighter as  $(N_{\text{tot}}, K_{\text{sel}})$  increases. This behavior is consistent with the theoretical development in Section III, since the proposed moment-matching MGF analysis relies

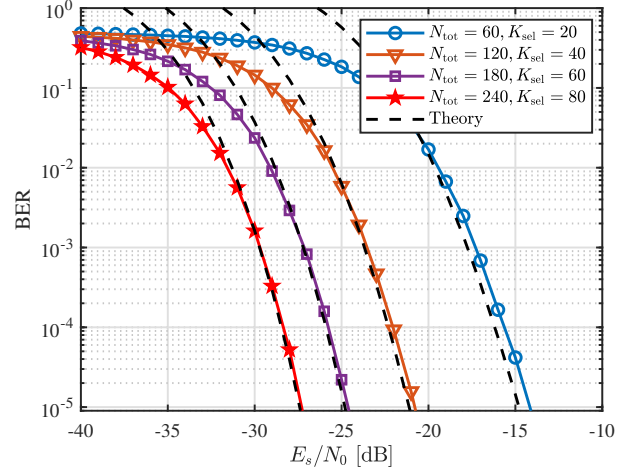


Fig. 4. BER performance comparison of the proposed FRIS-RSM under different  $K_{\text{sel}}$ , with a fixed activation ratio  $p_{\text{sel}} = K_{\text{sel}}/N_{\text{tot}} = 1/3$  and parameters  $(N_x, N_z, W_x, W_z) = (24, 10, 46\lambda, 18\lambda)$ ,  $M = 4$ ,  $N_r = 8$ , and  $Q = 3$ .

on the CLT approximation, whose accuracy improves as the number of combined cascaded paths becomes larger. Hence, Fig. 4 not only demonstrates the BER gain brought by larger FRIS configurations, but also confirms the increasing accuracy of the analytical approximation in the large- $K_{\text{sel}}$  regime.

Fig. 5 evaluates the quantized-phase FRIS-RSM scheme with  $Q = 3$  under  $(N_x, N_z, W_x, W_z) = (24, 10, 46\lambda, 18\lambda)$ , where  $M = 4$  and  $N_r = 8$ . The BER performance is reported for  $K_{\text{sel}} \in \{40, 80, 120, 160, 200, 240\}$  with a fixed fluid-element grid size  $N_{\text{tot}} = 240$ . At a target BER of  $10^{-4}$ , the configurations with  $K_{\text{sel}} = 40, 80, 120, 160$ , and  $200$  incur SNR losses of 8.16 dB, 4.18 dB, 2.13 dB, 0.98 dB, and 0.35 dB, respectively, compared with the full-activation benchmark  $K_{\text{sel}} = N_{\text{tot}} = 240$ . It is observed that increasing  $K_{\text{sel}}$  consistently improves the BER performance, but the incremental gain gradually diminishes as  $K_{\text{sel}}$  approaches  $N_{\text{tot}}$ . This trend reveals an important hardware implication: near-full-activation reliability can already be achieved by activating only a moderate subset of fluid elements, rather than all available candidates. Therefore, a favorable hardware-performance tradeoff can be obtained by properly choosing  $K_{\text{sel}}$ , thereby reducing the number of required RF control links and the associated implementation cost. In addition, for the entire range of activation ratios  $K_{\text{sel}}/N_{\text{tot}}$ , the analytical results closely match the simulated curves, which further validates the effectiveness of the proposed performance analysis under practical finite-resolution phase control.

Fig. 6 presents the BER performance of the quantized-phase FRIS-RSM scheme under different values of  $L$ . The simulation parameters are  $(N_x, N_z, W_x, W_z) = (20, 9, 4.5\lambda, 3\lambda)$ ,  $N_r = 16$ ,  $M = 16$ ,  $K_{\text{sel}} = 70$ , and  $Q = 2$ . The BER performance is evaluated for different list sizes  $L \in \{1, 2, 3, 5, 16\}$  in the proposed reduced-complexity list detector. The case  $L = 1$  corresponds to greedy detection, whereas  $L = N_r = 16$  reduces to the full ML detector. The simulation results show that, compared with the ML benchmark ( $L = 16$ ), the perfor-

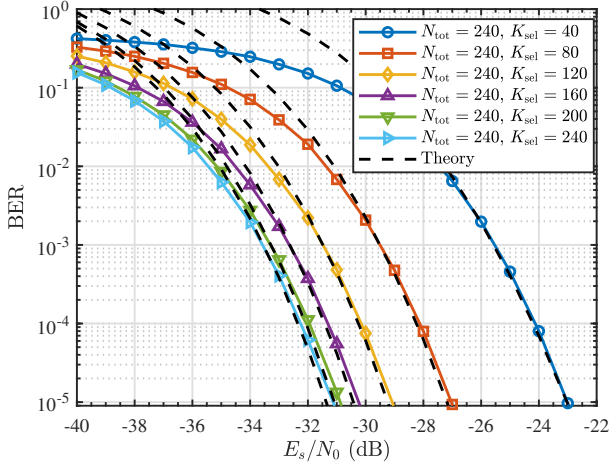


Fig. 5. BER performance comparison of the proposed FRIS-RSM under different activation ratios  $p_{\text{sel}} = K_{\text{sel}}/N_{\text{tot}}$ , with parameters  $N_{\text{tot}} = 240$ ,  $(N_x, N_z, W_x, W_z) = (24, 10, 46\lambda, 18\lambda)$ ,  $M = 4$ ,  $N_r = 8$ , and  $Q = 3$ .

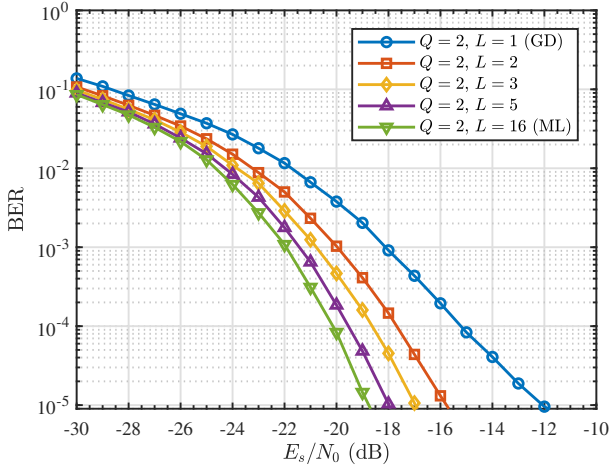


Fig. 6. Reduced-complexity list detection performance of the proposed FRIS-RSM over different  $L$  values, with parameters  $(N_x, N_z, W_x, W_z) = (20, 9, 4.5\lambda, 3\lambda)$ ,  $N_r = 16$ ,  $M = 16$ , and  $K_{\text{sel}} = 70$ .

performance losses for  $L = 1, 2, 3$ , and  $5$  are approximately 4.9 dB, 2.45 dB, 1.5 dB, and 0.59 dB, respectively. As expected, the BER performance improves monotonically as  $L$  increases. More importantly, the gain is substantial when  $L$  increases from very small values, whereas the marginal improvement becomes progressively smaller as  $L$  approaches  $N_r$ . This result shows that the proposed energy-based candidate selection can effectively compress the search space of receive antennas and thereby reduce the detection complexity with only a modest BER loss, provided that a moderate list size is adopted. Hence, the two-stage Top- $L$  detector offers an effective practical compromise between the simplicity of greedy detection and the optimality of full ML detection.

## V. CONCLUSION

This paper introduced FRIS-based IM schemes, namely FRIS-RSM and FRIS-RSSK, which leverage the spatial reconfigurability of FRIS to improve diversity and spectral

efficiency. A two-stage Top- $L$  detector was proposed, offering a complexity-performance tradeoff between greedy and ML detection. We derived the first- and second-order moments for the cascaded double-Rayleigh fading channels and formulated the UPEP and union-bound BER using an MGF-based approach. Simulation results validated the accuracy of the analysis, showing that the proposed FRIS-based schemes significantly outperform conventional RIS-based solutions. These results confirm the potential of FRIS in enhancing future wireless communication systems with efficient IM.

## APPENDIX A

### UPEP MGF AND BER LOWER BOUND WITH $\mathbf{J} = \mathbf{I}$

We show that among all Hermitian  $\mathbf{J} \succeq \mathbf{0}$  with unit diagonal,  $\mathbf{J} = \mathbf{I}$  minimizes the UPEP and hence provides a BER lower bound.

#### A. MGF reduction to a quadratic form

Recall  $\mathcal{Z}_{i,\hat{i}}^{x,\hat{x}} = \|\mathbf{d}\|_2^2$ , where  $\mathbf{d} = \mathbf{G}\mathbf{J}^{1/2}\mathbf{u}$  and  $\mathbf{u} \triangleq \Phi_i \mathbf{f}x - \Phi_{\hat{i}} \mathbf{f}\hat{x}$ . Conditioned on  $(\mathbf{u}, \mathbf{J})$ , each row  $\mathbf{g}_\ell$  of  $\mathbf{G}$  gives  $d_\ell = \mathbf{g}_\ell \mathbf{J}^{1/2} \mathbf{u} \sim \mathcal{CN}(0, \sigma_J^2)$  with  $\sigma_J^2 = \mathbf{u}^H \mathbf{J} \mathbf{u}$ . Hence  $\mathcal{Z}_{i,\hat{i}}^{x,\hat{x}} | (\mathbf{u}, \mathbf{J}) = \sum_{\ell=1}^{N_r} |d_\ell|^2$  is Gamma distributed with MGF

$$\mathbb{E}_{\mathbf{G}} \left[ e^{-s \mathcal{Z}_{i,\hat{i}}^{x,\hat{x}}} | \mathbf{u}, \mathbf{J} \right] = (1 + s \mathbf{u}^H \mathbf{J} \mathbf{u})^{-N_r}, \quad s \geq 0. \quad (79)$$

Let  $\mathbf{u} = \mathbf{A}\mathbf{f}$  with  $\mathbf{A} \triangleq \text{diag}(x\mathbf{v}_i - \hat{x}\mathbf{v}_{\hat{i}})$  and define  $\mathbf{B}_J \triangleq \mathbf{A}^H \mathbf{J} \mathbf{A} \succeq \mathbf{0}$ . Averaging (79) over  $\mathbf{f} \sim \mathcal{CN}(\mathbf{0}, \mathbf{I})$  yields

$$\mathcal{M}_{i,\hat{i}}^{x,\hat{x}}(s; \mathbf{J}) = \mathbb{E}_{\mathbf{f}} \left[ (1 + s \mathbf{f}^H \mathbf{B}_J \mathbf{f})^{-N_r} \right], \quad s \geq 0. \quad (80)$$

#### B. Schur-convex ordering and the $\mathbf{J} = \mathbf{I}$ bound

Since  $\text{diag}(\mathbf{J}) = \mathbf{1}$ , we have  $\text{diag}(\mathbf{B}_J) = \text{diag}(\mathbf{A}^H \mathbf{A}) \triangleq \mathbf{b}$ . For  $\mathbf{J} = \mathbf{I}$ , it follows that  $\mathbf{B}_I = \mathbf{A}^H \mathbf{A} = \text{diag}(\mathbf{b})$ . Let  $\lambda(\mathbf{B}_J) = (\lambda_1, \dots, \lambda_{N_{\text{tot}}})$  denote the eigenvalues of  $\mathbf{B}_J$ . By the Schur-Horn theorem, any Hermitian matrix with diagonal  $\mathbf{b}$  satisfies

$$\lambda(\mathbf{B}_J) \succ \mathbf{b} = \lambda(\mathbf{B}_I). \quad (81)$$

Using the unitary invariance of  $\mathbf{f}$ ,  $\mathbf{f}^H \mathbf{B}_J \mathbf{f} = \sum_k \lambda_k |z_k|^2$  with  $z_k \sim \mathcal{CN}(0, 1)$  i.i.d. Thus (80) becomes a symmetric function of  $\lambda(\mathbf{B}_J)$ ,

$$\mathcal{M}_{i,\hat{i}}^{x,\hat{x}}(s; \mathbf{J}) = \mathbb{E}_{\mathbf{z}} \left[ \left( 1 + s \sum_{k=1}^{N_{\text{tot}}} \lambda_k |z_k|^2 \right)^{-N_r} \right]. \quad (82)$$

For fixed  $\mathbf{z}$ , define  $g(x) = (1 + sx)^{-N_r}$  for  $x \geq 0$ . Since  $g''(x) = N_r(N_r + 1)s^2(1 + sx)^{-N_r-2} > 0$ ,  $g(x)$  is decreasing and convex. Hence (82) is a symmetric convex function of the eigenvalue vector, i.e., Schur-convex. Combining this property with (81) gives

$$\mathcal{M}_{i,\hat{i}}^{x,\hat{x}}(s; \mathbf{J}) \geq \mathcal{M}_{i,\hat{i}}^{x,\hat{x}}(s; \mathbf{I}), \quad s \geq 0. \quad (83)$$

Finally, the UPEP in (31) is a positive-weight integral of  $\mathcal{M}_{i,\hat{i}}^{x,\hat{x}}(s; \mathbf{J})$  for  $s > 0$  (and similarly for (32)). Therefore,  $\overline{P}(i, x \rightarrow \hat{i}, \hat{x} | \mathbf{J}) \geq \overline{P}(i, x \rightarrow \hat{i}, \hat{x} | \mathbf{I})$ . Since the BER union bound is a positive weighted sum of UPEPs,  $\mathbf{J} = \mathbf{I}$  yields a BER lower bound.

## REFERENCES

- [1] W. K. New, K.-K. Wong, H. Xu, C. Wang, F. R. Ghadi, J. Zhang, J. Rao, R. Murch, P. Ramirez-Espinosa, D. Morales-Jimenez, C.-B. Chae, and K.-F. Tong, "A tutorial on fluid antenna system for 6G networks: Encompassing communication theory, optimization methods and hardware designs," *IEEE Commun. Surv. Tuts.*, vol. 27, no. 4, pp. 2325–2377, Aug. 2025.
- [2] T. Wu, K. Zhi, J. Yao, X. Lai, J. Zheng, H. Niu, M. Elkaslan, K.-K. Wong, C.-B. Chae, Z. Ding, G. K. Karagiannidis, M. Debbah, and C. Yuen, "Fluid Antenna Systems enabling 6G: Principles, applications, and research directions," *IEEE Wireless Commun.*, early access, 2025, doi:[10.1109/MWC.2025.3629597](https://doi.org/10.1109/MWC.2025.3629597).
- [3] W.-J. Lu, C.-X. He, Y. Zhu, K.-F. Tong, K.-K. Wong, H. Shin, and T. J. Cui, "Fluid antennas: Reshaping intrinsic properties for flexible radiation characteristics in intelligent wireless networks," *IEEE Commun. Mag.*, vol. 63, no. 5, pp. 40–45, May 2025.
- [4] H. Hong, K.-K. Wong, C.-B. Chae, H. Xu, X. Guo, F. R. Ghadi, Y. Chen, Y. Xu, B. Liu, K.-F. Tong, and Y. Zhang, "A contemporary survey on fluid antenna systems: Fundamentals and networking perspectives," *IEEE Trans. Netw. Sci. Eng.*, vol. 13, pp. 2305–2328, 2026.
- [5] Z. Zhang, K.-K. Wong, D. Morales-Jimenez, H. Jiang, P. Ramirez-Espinosa, C.-B. Chae, and C. Masouros, "Finite-blocklength fluid antenna systems with spatial block-correlation channel model," *IEEE Wireless Commun. Lett.*, vol. 15, pp. 1911–1915, 2026.
- [6] L. Zhu, W. Ma, and R. Zhang, "Movable antennas for wireless communication: Opportunities and challenges," *IEEE Commun. Mag.*, vol. 62, no. 6, pp. 114–120, Jun. 2024.
- [7] J. O. Martinez, J. R. Rodríguez, Y. Shen, K.-F. Tong, K.-K. Wong, and A. G. Armada, "Toward liquid reconfigurable antenna arrays for wireless communications," *IEEE Commun. Mag.*, vol. 60, no. 12, pp. 145–151, Dec. 2022.
- [8] J. Zhang, J. Rao, Z. Li, Z. Ming, C.-Y. Chiu, K.-K. Wong, K.-F. Tong, and R. Murch, "A novel pixel-based reconfigurable antenna applied in fluid antenna systems with high switching speed," *IEEE Open J. Antennas Propag.*, vol. 6, no. 1, pp. 212–228, Feb. 2025.
- [9] K.-K. Wong, C. Wang, S. Shen, C.-B. Chae, and R. Murch, "Reconfigurable pixel antennas meet fluid antenna systems: A paradigm shift to electromagnetic signal and information processing," *IEEE Wireless Commun.*, vol. 33, no. 1, pp. 191–198, Feb. 2026.
- [10] W. K. New, K.-K. Wong, C. Wang, C.-B. Chae, R. Murch, H. Jafarkhani, and Y. Hao, "Fluid antenna systems: Redefining reconfigurable wireless communications," *IEEE J. Sel. Areas Commun.*, vol. 44, pp. 1013–1044, 2026.
- [11] Z. Zhang, K.-K. Wong, J. Dang, Z. Zhang, and C.-B. Chae, "On fundamental limits for fluid antenna-assisted integrated sensing and communications for unsourced random access," *IEEE J. Sel. Areas Commun.*, vol. 44, pp. 136–149, 2026.
- [12] K.-K. Wong and K.-F. Tong, "Fluid antenna multiple access," *IEEE Trans. Wireless Commun.*, vol. 21, no. 7, pp. 4801–4815, Jul. 2022.
- [13] Z. Zhang, K.-K. Wong, J. Dang, Z. Zhang, C. Masouros, and C.-B. Chae, "On fundamental limits of slow-fluid antenna multiple access for unsourced random access," *IEEE Wireless Commun. Lett.*, vol. 14, no. 11, pp. 3455–3459, Nov. 2025.
- [14] T. Han, Y. Zhu, K.-K. Wong, G. Zheng, and H. Shin, "Cell-free fluid antenna multiple access networks," *IEEE Trans. Wireless Commun.*, vol. 24, no. 9, pp. 7237–7251, Sept. 2025.
- [15] T. Hao, C. Shi, Q. Wu, B. Xia, Y. Guo, L. Ding, and F. Yang, "Fluid-antenna enhanced ISAC: Joint antenna positioning and dual-functional beamforming design under perfect and imperfect CSI," *IEEE Trans. Veh. Technol.*, vol. 74, no. 11, pp. 17 204–17 219, Nov. 2025.
- [16] J. Ye, J. Dai, K. Wang, and F. Zhang, "Fluid antennas enabled integrated sensing and communication," *IEEE Wireless Commun. Lett.*, vol. 14, no. 8, pp. 2641–2645, Aug. 2025.
- [17] J. Li, L. Yang, C. You, I. Ahmad, P. S. Bithas, M. Di Renzo, and D. Niyato, "Absorptive RIS-assisted near-field covert communication with fluid antenna systems," *IEEE J. Sel. Areas Commun.*, vol. 44, pp. 2052–2070, 2026.
- [18] Y. Chen, M. Chen, H. Xu, Z. Yang, K.-K. Wong, and Z. Zhang, "Joint beamforming and antenna design for near-field fluid antenna system," *IEEE Wireless Commun. Lett.*, vol. 14, no. 2, pp. 415–419, Feb. 2025.
- [19] P. Zhang, J. Dang, M. Wen, Z. Liu, C. Zhao, H. Shi, C. Pan, and Z. Zhang, "Artificial noise aided physical layer security for near-field MIMO with fluid antenna systems," 2025, arXiv:[2512.02461](https://arxiv.org/abs/2512.02461).
- [20] F. Rostami Ghadi, K.-K. Wong, W. K. New, H. Xu, R. Murch, and Y. Zhang, "On performance of RIS-aided fluid antenna systems," *IEEE Wireless Commun. Lett.*, vol. 13, no. 8, pp. 2175–2179, Aug. 2024.
- [21] C. Wang, Z. Li, K.-K. Wong, R. Murch, C.-B. Chae, and S. Jin, "AI-empowered fluid antenna systems: Opportunities, challenges, and future directions," *IEEE Wireless Commun.*, vol. 31, no. 5, pp. 34–41, Oct. 2024.
- [22] H. Yang, H. Xu, K. Wong, C. Chae, R. Murch, S. Jin, and Y. Zhang, "Position index modulation for fluid antenna system," *IEEE Trans. Wireless Commun.*, vol. 23, no. 11, pp. 16 773–16 787, Nov. 2024.
- [23] J. Zhu, G. Chen, P. Gao, P. Xiao, Z. Lin, and A. U. Qaddus, "Index modulation for fluid antenna-assisted MIMO communications: System design and performance analysis," *IEEE Trans. Wireless Commun.*, vol. 23, no. 8, pp. 9701–9713, Aug. 2024.
- [24] X. Guo, Y. Xu, D. He, C. Zhang, H. Hong, K. Wong, W. Zhang, and Y. Wu, "Fluid antenna index modulation for MIMO systems: Robust transmission and low-complexity detection," *IEEE Trans. Commun.*, vol. 73, no. 12, pp. 15 955–15 970, Dec. 2025.
- [25] E. Faddoul, G. M. Kraidy, C. Psomas, and I. Krikidis, "Advanced channel coding designs for index-modulated fluid antenna systems," *IEEE Trans. Commun.*, vol. 73, no. 2, pp. 726–739, Feb. 2025.
- [26] P. Zhang, J. Dang, M. Wen, Z. Zhang, L. Wu, and Y. Yao, "Fluid antenna-assisted rectangular differential index modulation: A non-coherent system design, optimization, and performance analysis," *IEEE J. Sel. Areas Commun.*, vol. 44, pp. 1307–1321, 2026.
- [27] M. Liu, Y. Xiao, L. Zhang, S. Yang, C. Wu, and X. Lei, "Index modulation for covert transmission in continuous-trajectory fluid antenna systems," *IEEE Trans. Veh. Technol.*, early access 2025, doi:[10.1109/TVT.2025.3612838](https://doi.org/10.1109/TVT.2025.3612838).
- [28] E. Basar, "Reconfigurable intelligent surface-based index modulation: A new beyond MIMO paradigm for 6G," *IEEE Trans. Commun.*, vol. 68, no. 5, pp. 3187–3196, May 2020.
- [29] T. Ma, "Large intelligent surface assisted wireless communications with spatial modulation and antenna selection," *IEEE J. Sel. Areas Commun.*, vol. 38, no. 11, pp. 2562–2574, Nov. 2020.
- [30] J. Yuan, M. Wen, Q. Li, E. Basar, G. C. Alexandropoulos, and G. Chen, "Receive quadrature reflecting modulation for RIS-empowered wireless communications," *IEEE Trans. Veh. Technol.*, vol. 70, no. 5, pp. 5121–5125, May 2021.
- [31] M. H. Dinan, N. S. Perović, and M. F. Flanagan, "RIS-assisted receive quadrature space-shift keying: A new paradigm and performance analysis," *IEEE Trans. Commun.*, vol. 70, no. 10, pp. 6874–6889, Oct. 2022.
- [32] P. A. Marín, M. Hanif, and E. Bedeer, "RIS-assisted receive generalized space-shift keying and receive generalized spatial modulation," *IEEE Wireless Commun. Lett.*, vol. 13, no. 10, pp. 2712–2716, Oct. 2024.
- [33] M. Yue, Y. Peng, R. Ye, H. Hai, F. Al-Hazemi, and J. Lee, "IRS-assisted extended variable spatial modulation: A high spectral efficiency scheme," *IEEE Wireless Commun. Lett.*, vol. 13, no. 7, pp. 1838–1842, Jul. 2024.
- [34] A. T. Dogukan, E. Arslan, M. E. Pihitili, and E. Basar, "RIS-aided enhanced receive spatial modulation," *IEEE Wireless Commun. Lett.*, vol. 14, no. 1, pp. 188–192, Jan. 2025.
- [35] M. Yue, Y. Peng, Q. Jin, and J. Lee, "RIS-assisted flexible receive spatial modulation for wireless communication," *IEEE Wireless Commun. Lett.*, vol. 14, no. 7, pp. 1859–1863, Jul. 2025.
- [36] J. Zhu, Q. Luo, G. Chen, P. Xiao, Y. Xiao, and K. K. Wong, "Fluid antenna empowered index modulation for RIS-aided mmwave transmissions," *IEEE Trans. Wireless Commun.*, vol. 24, no. 2, pp. 1635–1647, Feb. 2025.
- [37] A. Salem, K.-K. Wong, G. Alexandropoulos, C.-B. Chae, and R. Murch, "A first look at the performance enhancement potential of fluid reconfigurable intelligent surface," 2025, arXiv:[2502.17116](https://arxiv.org/abs/2502.17116).
- [38] H. Xiao, X. Hu, K.-K. Wong, X. Zhu, H. Hong, and C.-B. Chae, "Fluid reconfigurable intelligent surface with element-level pattern reconfigurability: Beamforming and pattern co-design," *IEEE Trans. Wireless Commun.*, vol. 25, pp. 10 791–10 806, 2026.
- [39] J. D. Vega Sánchez, V. H. G. Pacheco, N. V. Orozco Garzón, H. R. Carvajal Mora, and F. J. López-Martínez, "Understanding the role of phase and position design in fluid reconfigurable intelligent surfaces," *IEEE Open J. Commun. Soc.*, vol. 7, pp. 1414–1425, 2026.
- [40] H. Xiao, X. Hu, K.-K. Wong, H. Hong, G. C. Alexandropoulos, and C.-B. Chae, "Fluid reconfigurable intelligent surfaces: Joint on-off selection and beamforming with discrete phase shifts," *IEEE Wireless Commun. Lett.*, vol. 14, no. 10, pp. 3124–3128, oct. 2025.
- [41] F. Rostami Ghadi, K.-K. Wong, F. J. López-Martínez, G. C. Alexandropoulos, and C.-B. Chae, "Performance analysis of wireless communication systems assisted by fluid reconfigurable intelligent surfaces," *IEEE Wireless Commun. Lett.*, vol. 14, no. 12, pp. 3922–3926, Dec. 2025.
- [42] W. Sun, S. Sun, T. Shi, X. Su, and R. Liu, "Holographic communications enabled by fluid RIS: Holographic parameter reconstruction and

- beamforming.” *IEEE J. Sel. Areas Commun.*, vol. 44, pp. 1432–1448, 2026.
- [43] M. Kaveh, F. Rostami Ghadi, F. Hernando-Gallego, D. Martín, K.-K. Wong, and R. Jäntti, “Physical layer security over fluid reconfigurable intelligent surface-assisted communication systems,” *IEEE Wireless Commun. Lett.*, vol. 15, pp. 1697–1701, 2026.
- [44] J. D. Vega-Sánchez, V. H. G. Pacheco, N. V. O. Garzón, D. A. R. Almeida, and D. P. M. Osorio, “Exploring spatial flexibility and phase design in fluid reconfigurable intelligent surfaces: A physical layer security perspective,” *IEEE Open J. Commun. Soc.*, vol. 7, pp. 965–977, 2026.
- [45] W. K. New, K.-K. Wong, H. Xu, K.-F. Tong, and C.-B. Chae, “An information-theoretic characterization of MIMO-FAS: Optimization, diversity-multiplexing tradeoff and  $q$ -outage capacity,” *IEEE Trans. Wireless Commun.*, vol. 23, no. 6, pp. 5541–5556, Jun. 2024.